Supplementary Information (SI) for Journal of Materials Chemistry A.

Electronic supplementary information

High-density single-atom vanadium catalysts for efficient capture and bidirectional conversion of polysulfides in lithium-sulfur batteries

Qingqing Chen,[‡a,b] Jianguo Si,[‡a,b] Haoliang Huang,[a] Wei Wang,[a,b] Weicai Zhang,[a,b]
Sheng Meng,[*b] and Lifeng Liu[*a]

[a] Songshan Lake Materials Laboratory (SLAB), Dongguan 523808, P. R. China

[b] Institute of Physics, Chinese Academy of Sciences, Beijing 100190, P. R. China

[*]Corresponding author.

E-mail address: liu.lifeng@sslab.org.cn (L. Liu) and smeng@iphy.ac.cn (S. Meng)

[‡] Q. Chen and J. Si contributed equally to this work.

Supplementary methods

Visual LiPSs adsorption tests

Li_2S_6 was selected as a representative of LiPSs to perform the adsorption tests. The Li_2S_6 solution was prepared by dissolving Li_2S and S (1:5, molar ratio) in the mixture of DME/DOL (1:1, v/v) solvents, leading to a concentration of 4.0 mM. Afterward, 20 mg of HD-V-SACs or NC were added into 2.5 mL Li_2S_6 solution. The adsorption tests were carried out in an Ar-filled glove box (Mbraun).

Assembly of symmetric cells

The slurry was obtained by adding the as-prepared catalysts and PVDF (8:2, mass ratio) into N-methyl-2-pyrrolidone (NMP), followed by agitation at room temperature for 0.5 h. The electrode sheets were then prepared by coating the slurry onto a carbon-coated aluminum (Al) foil that was subsequently dried at 60 °C for 12 h in vacuum. The electrode sheet was cut into circular disks of 12 mm in diameter with a mass loading of ~0.8 mg cm^{-2}. CR2032-type symmetric cells were assembled in an Ar-filled glove box (Mbraun) using the two pieces of identical electrode disks as the working and counter electrodes, 30 μL of 0.5 M Li_2S_6 as the electrolyte and a Celgard-2500 membrane as the separator. The Li_2S_6 electrolyte was obtained by dissolving Li_2S and S (1:5, molar ratio) in the mixture of DME/DOL (1:1, v/v) and 1 M LiTFSI. Cyclic voltammetry (CV) measurements of the symmetrical cells were conducted at a scan rate of 5 mV s^{-1} in the potential window of $-1.0 \sim 1.0$ V.

Li_2S nucleation and dissolution tests

0.2 M Li_2S_8 electrolyte was firstly prepared by dissolving Li_2S and S (1:7, molar ratio) in the mixture of DME/DOL (1:1, v/v) and 1 M LiTFSI. Li_2S nucleation experiments were performed in CR2032 coin cells consisting of the above-mentioned circular disk electrode as the cathode (diameter: 12 mm, mass loading: ~0.8 mg cm^{-2}), a Li foil as the anode, and a Celgard-2500 membrane as the separator. Specifically, 20 μL of 0.2 M Li_2S_8 electrolyte were spread onto the cathode, and then 20 μL traditional electrolyte (i.e., 1 M LiTFSI in DME/DOL (1:1, v/v) with 2 wt% $LiNO_3$) were drop-cast onto the Li anode. The cell was firstly discharged to 2.10 V at a current of 25 mA, and then potentiostatically discharged at 2.05 V until the current density decreased to 0.01 mA. For Li_2S dissolution measurements, the assembled cell was galvanostatically discharged to 1.80 V at 25 mA and then potentiostatically charged to 2.38 V until the charge current density was below 0.01 mA.

In-situ Raman spectroscopy measurements

The in-situ Raman spectroscopy measurements (Nanophoton, wavelength: 532 nm) were conducted using a home-made electrochemical cell with a transparent quartz window (Tianjin Aida Technology Co. Ltd). In this case, the Li foil counter electrode was placed close to the quartz window to facilitate the collection of LiPSs Raman signals from the anode side. To enable the laser to pass through the window to acquire Raman signals, a hole of 6 mm in diameter was opened in the Li foil (**Fig. 4d**). The Li-S cell was discharged at 0.5 C during the measurements.

Density functional theory (DFT) calculations

All calculations were performed based on the density functional theory (DFT) method under periodic boundary conditions, in complement to the Vienna Ab-initio Simulation

Package (VASP).[S1] The projector augmented wave (PAW) method with a generalized gradient approximation based on the Perdew-Burke-Erzerhof (PBE) exchange correlation functional was adopted. Integration in the Brillioiun zone was performed on the basis of the Monkhorst-Pack scheme using a Γ centered 3 × 3 × 1 k-point mesh in each primitive lattice vector of the reciprocal space for optimization. The convergence criterion for the electronic structure iteration was set to be 10^{-5} eV, and that for geometry optimization was set to be 0.05 eV $Å^{-1}$ on force. The plane-wave cutoff energy of 500 eV was used. Lattice parameters and internal atomic positions were fully optimized. The D3 method developed by Grimme[S2] was employed to describe the van der Waals (vdW) dispersion.

The reaction Gibbs free energy ΔG was defined as follows:

$$\Delta G = \Delta E + \Delta ZPE - T\Delta S \tag{S1}$$

where ΔE is the binding energy, ΔZPE represents the change in zero-point energy, T stands for the temperature, and ΔS denotes the entropy change. At low temperatures, the contribution of entropy to ΔG is small, and therefore the value of ΔS is set to zero.

A reduction process of S_8 to Li_2S can be expressed as follows:

$$S_8 + 2Li \overset{r_1}{\rightarrow} Li_2S_8 \overset{r_2}{\rightarrow} Li_2S_6 \overset{r_3}{\rightarrow} Li_2S_4 \overset{r_4}{\rightarrow} Li_2S_2 \overset{r_5}{\rightarrow} Li_2S \tag{S2}$$

Accordingly, the free energy change of each reaction step was calculated according to the following equations:

$$\Delta G_{r1} = E(*\,Li_2S_8) - E(*) - E(S_8) - 2E(Li) + G_{corr}(*\,Li_2S_8) \tag{S3}$$

$$\Delta G_{r2} = E(*\,Li_2S_6) - E(*\,Li_2S_8) + \frac{1}{4}E(S_8) + G_{corr}(*\,Li_2S_6) - G_{corr}(*\,Li_2S_8) \tag{S4}$$

$$\Delta G_{r3} = E(*\,Li_2S_4) - E(*\,Li_2S_6) + \frac{1}{4}E(S_8) + G_{corr}(*\,Li_2S_4) - G_{corr}(*\,Li_2S_6) \tag{S5}$$

$$\Delta G_{r4} = E(*\,Li_2S_2) - E(*\,Li_2S_4) + \frac{1}{4}E(S_8) + G_{corr}(*\,Li_2S_2) - G_{corr}(*\,Li_2S_4) \tag{S6}$$

$$\Delta G_{r5} = E(*\,Li_2S) - E(*\,Li_2S_2) + \frac{1}{8}E(S_8) + G_{corr}(*\,Li_2S) - G_{corr}(*\,Li_2S_2) \qquad \text{(S7)}$$

where $E(*Li_2S_x)$, $E(*)$, $E(Li)$ and $E(S_8)$ represent the energy values of $*Li_2S_x$ adsorbed on the slab, a clean slab, the bcc Li (per atom) and molecular S_8, respectively. $G_{corr}(*Li_2S_x)$ is the zero-point vibration energy calculated using vaspkit at $T = 298.15$ K.

The binding energy between the Li_2S_x ($x = 8, 6, 4, 2, 1$) and the substrate is defined as follows:

$$E_b = E(*\,Li_2S_X) - E(*) - E(Li_2S_X) \qquad \text{(S8)}$$

Self-consistent field calculations (SCF) were carried out until the SCF tolerance was below 1×10^{-5}. The binding energy was obtained by subtracting the SCF energies of both Li_2S_x and the slab from the SCF energy of the substrate with an adsorbed Li_2S_x intermediate. According to such a definition, a more negative value indicates a stronger bond between the Li_2S_x species and the metal center.

The climbing image nudged elastic band (CI-NEB) was applied to compute the decomposition barriers, which allows for obtaining the minimum energy path between the given initial and final positions.[S3]

Supplementary Figures

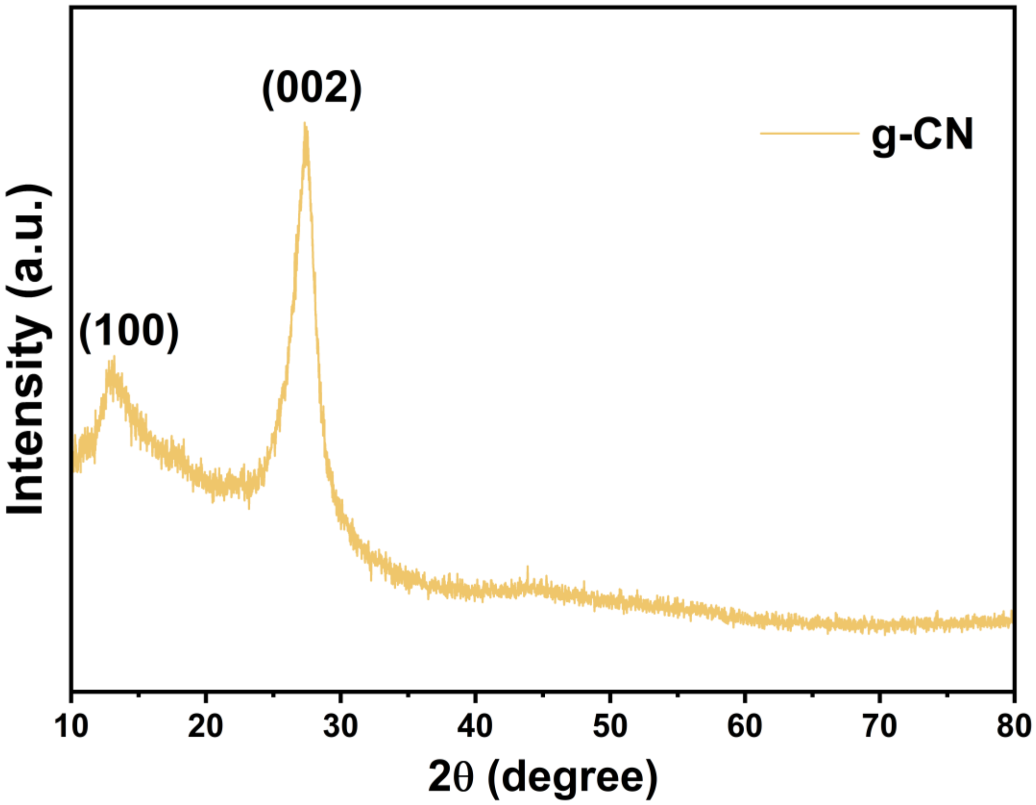

Fig. S1. XRD pattern of g-CN supports.

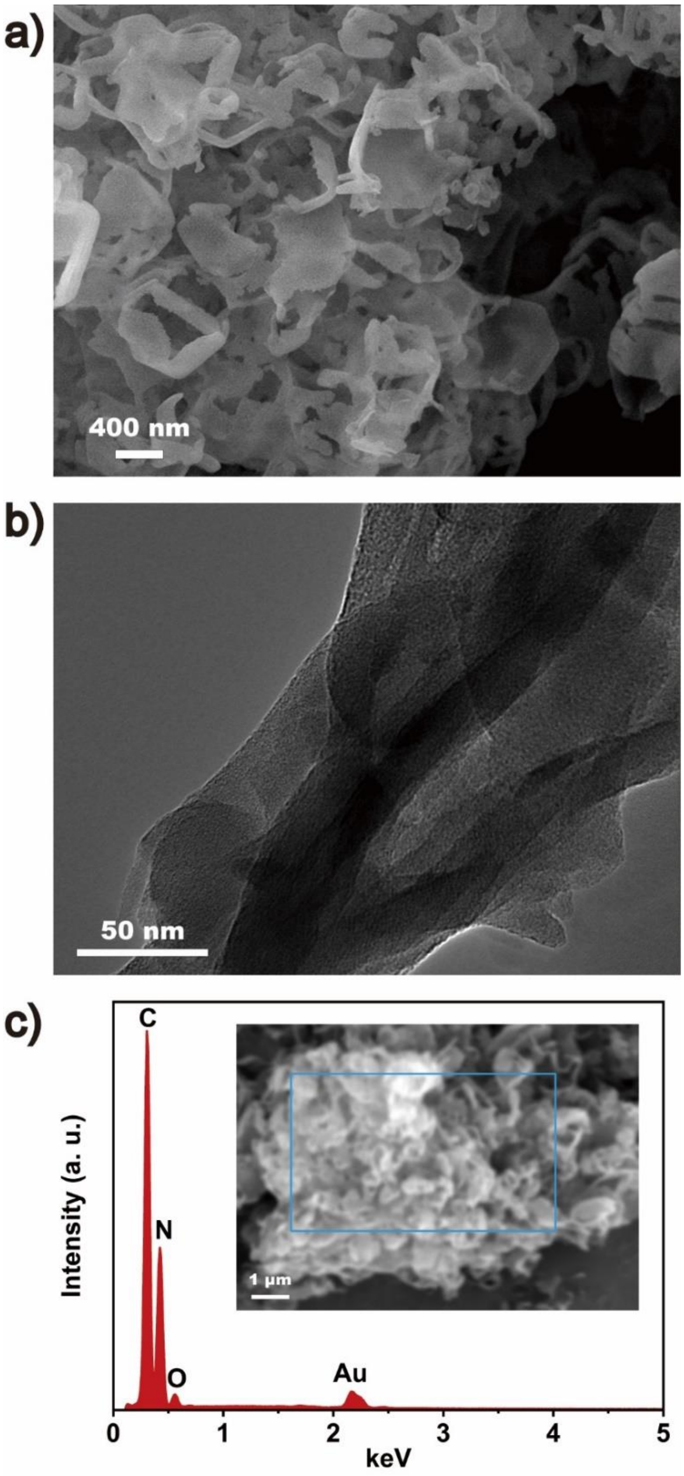

Fig. S2. (a) SEM, (b) TEM images, and (c) EDS spectrum (inset: corresponding SEM image) of g-CN supports. The Au peak comes from the sputtered Au film used to enhance SEM imaging.

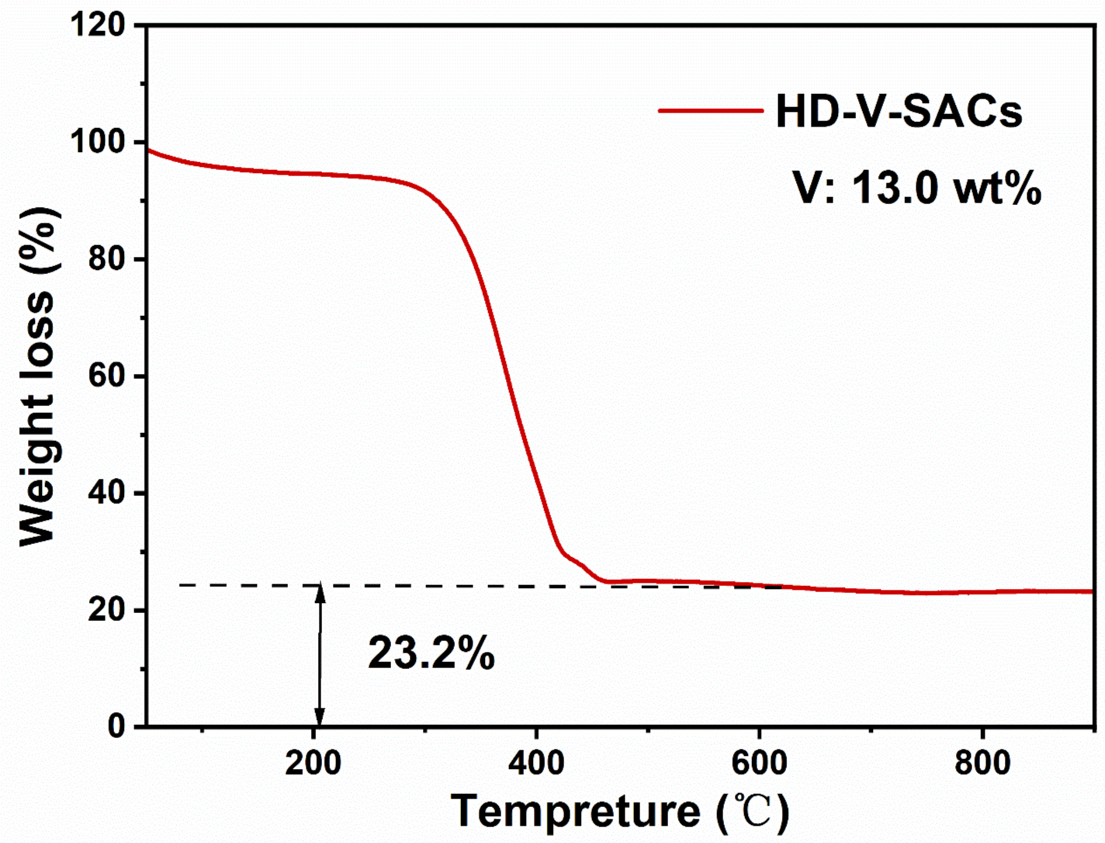

Fig. S3. TGA curve of HD-V-SACs, acquired in the temperature range from room temperature to 900 ℃ in air.

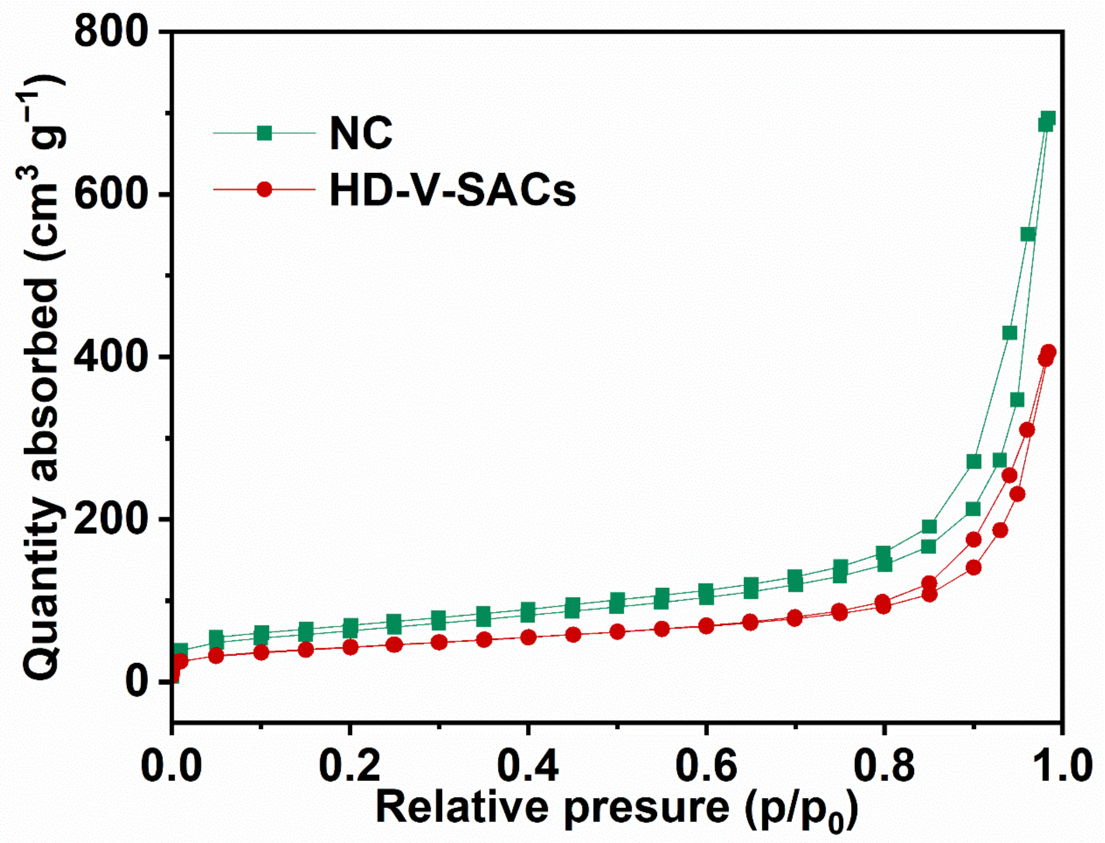

Fig. S4. The nitrogen adsorption/desorption isotherms of HD-V-SACs and NC.

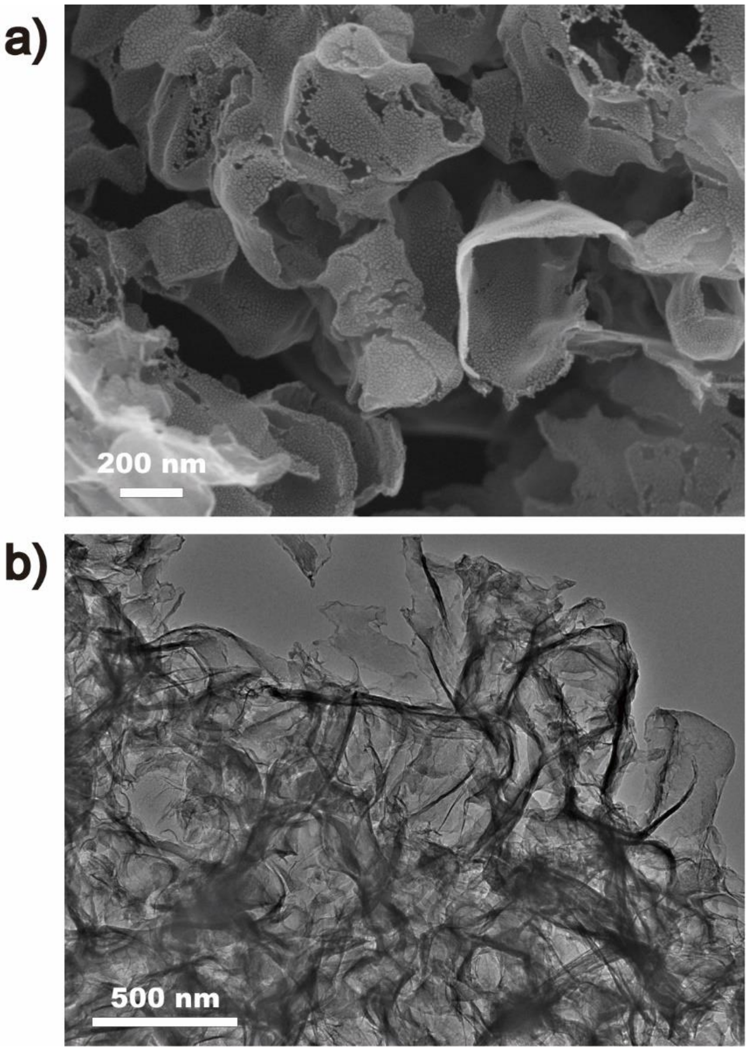

Fig. S5. (a) SEM and (b) TEM images of NC.

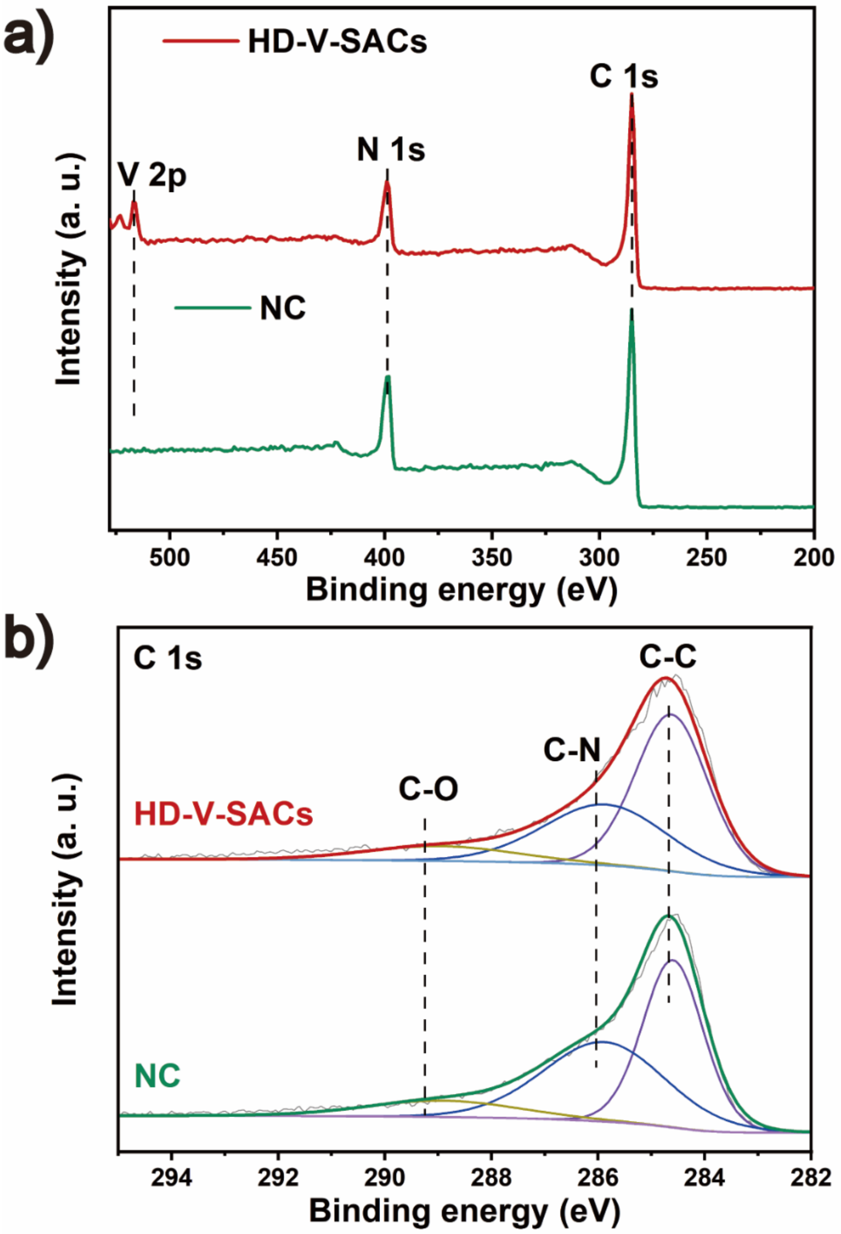

Fig. S6. (a) XPS survey spectra and (b) High-resolution C 1s XPS spectra of HD-V-SACs and NC.

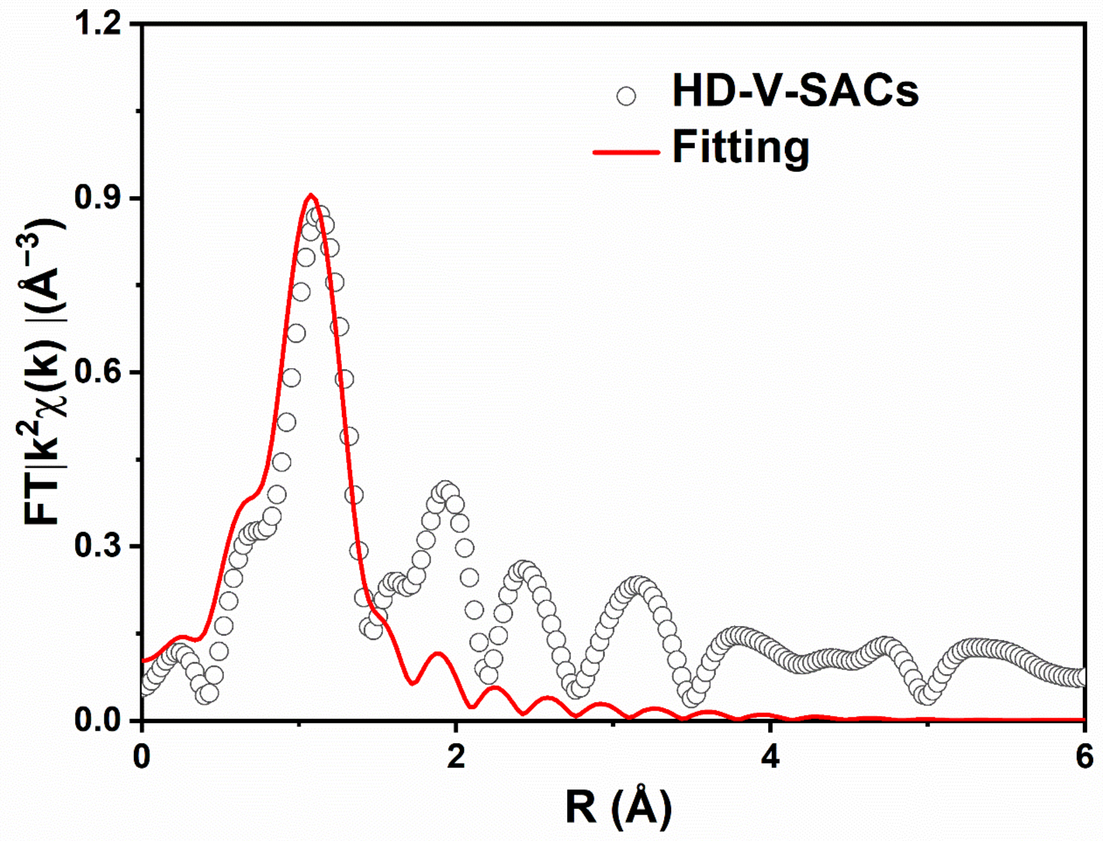

Fig. S7. FT-EXAFS spectrum of HD-V-SACs.

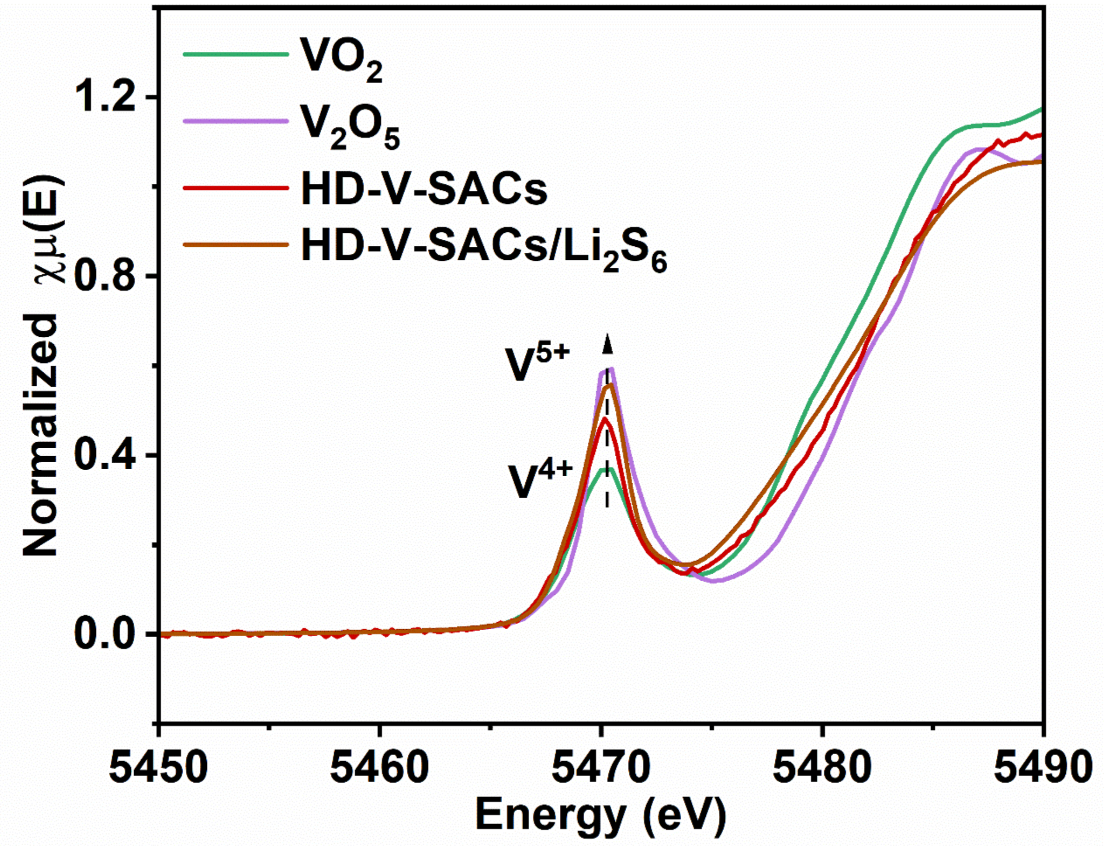

Fig. S8. V K-edge XANES spectra of HD-V-SACs before and after adsorbing Li_2S_6.

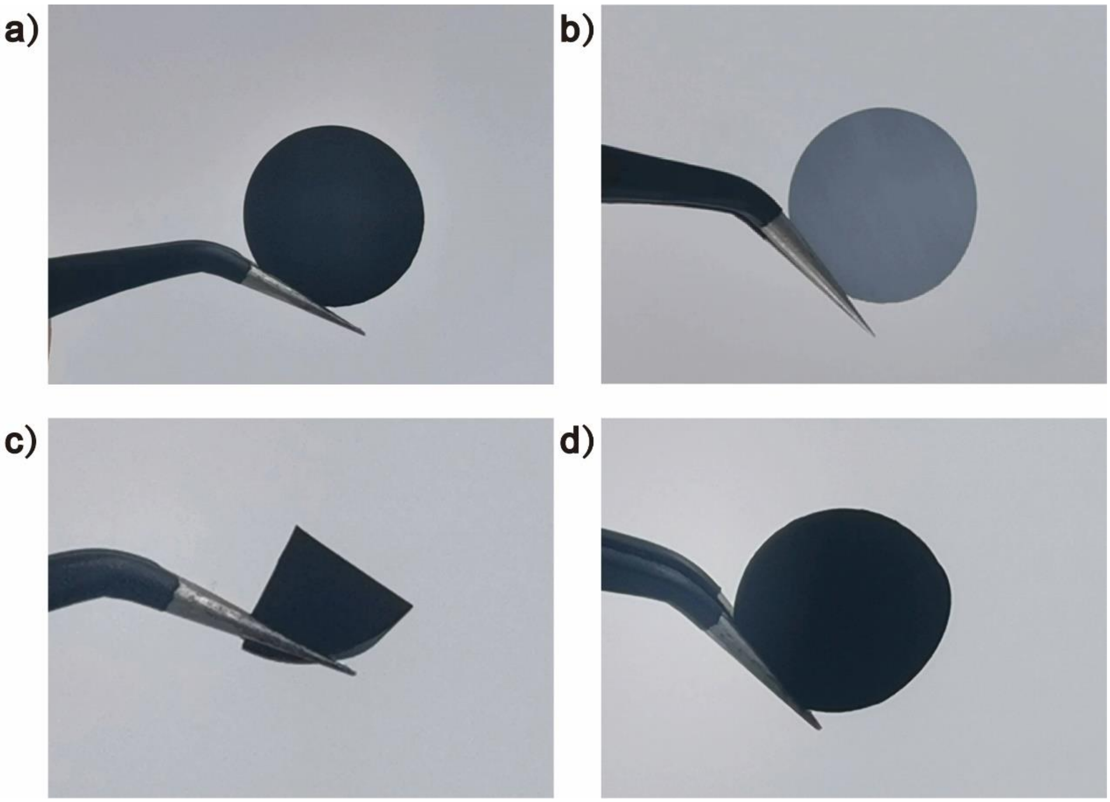

Fig. S9. Digital photographs showing the appearance of the surface of the HD-V-SACs/PP separator facing (a) the cathode and (b) the anode. Digital photographs illustrating the (c) folding and (d) unfolding states of the HD-V-SACs modified separator.

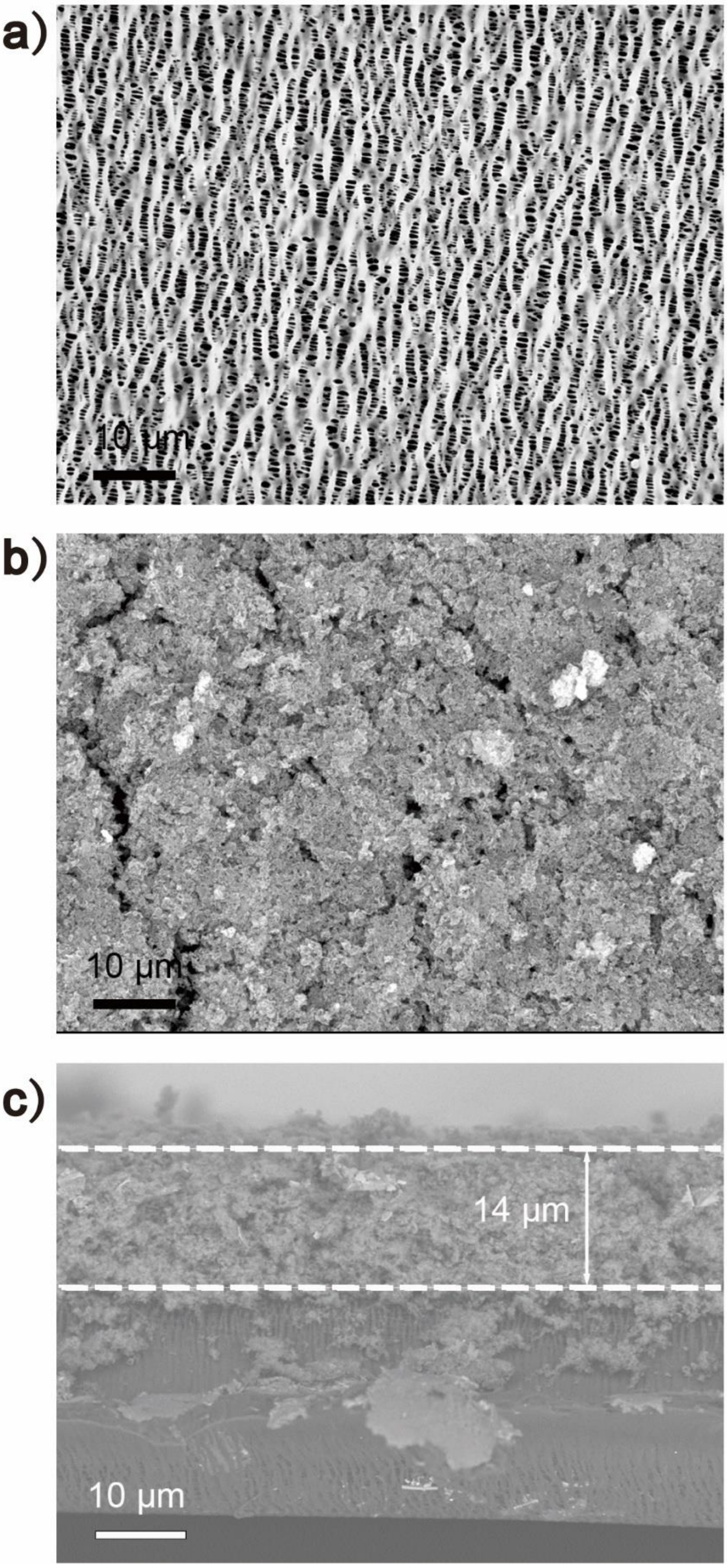

Fig. S10. SEM images showing the morphology of the surface of (a) the pristine PP separator and (b) the HD-V-SACs modified PP separator. (c) SEM image showing the morphology of the cross-section of HD-V-SACs/PP.

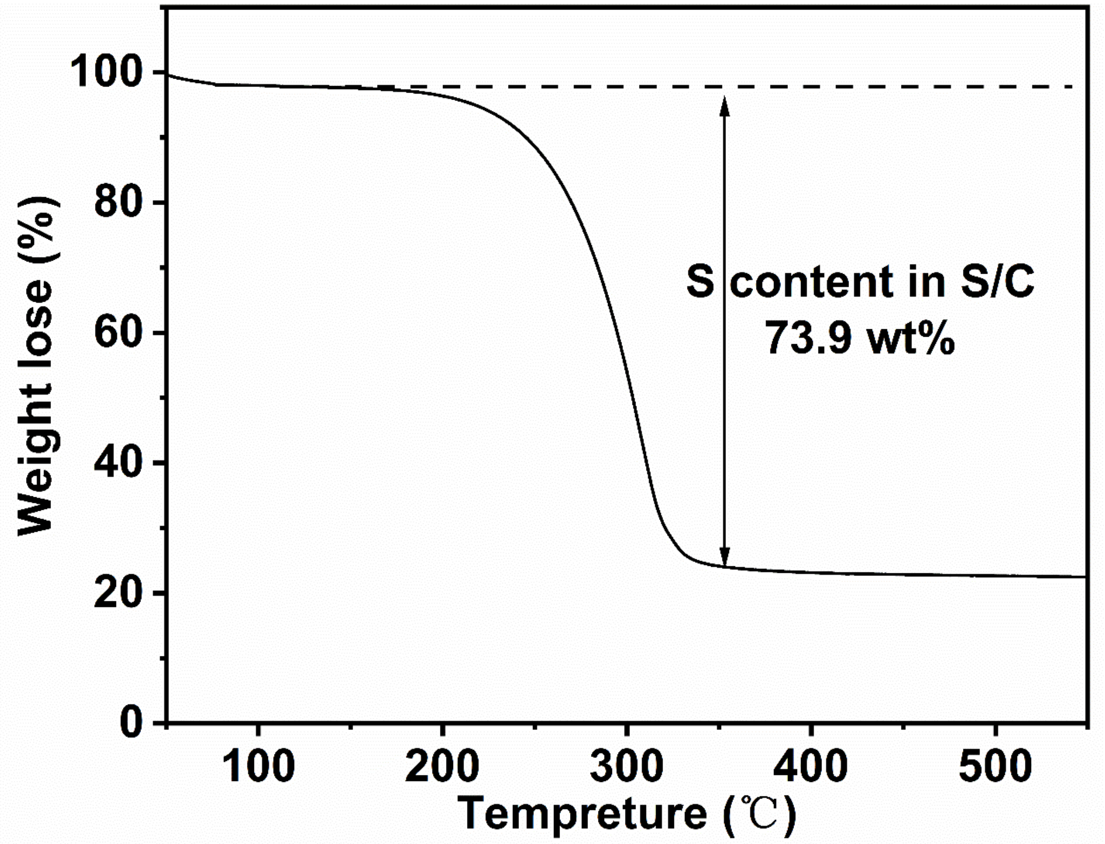

Fig. S11. TGA curve of S/C, acquired from room temperature to 600 °C in N_2 atmosphere.

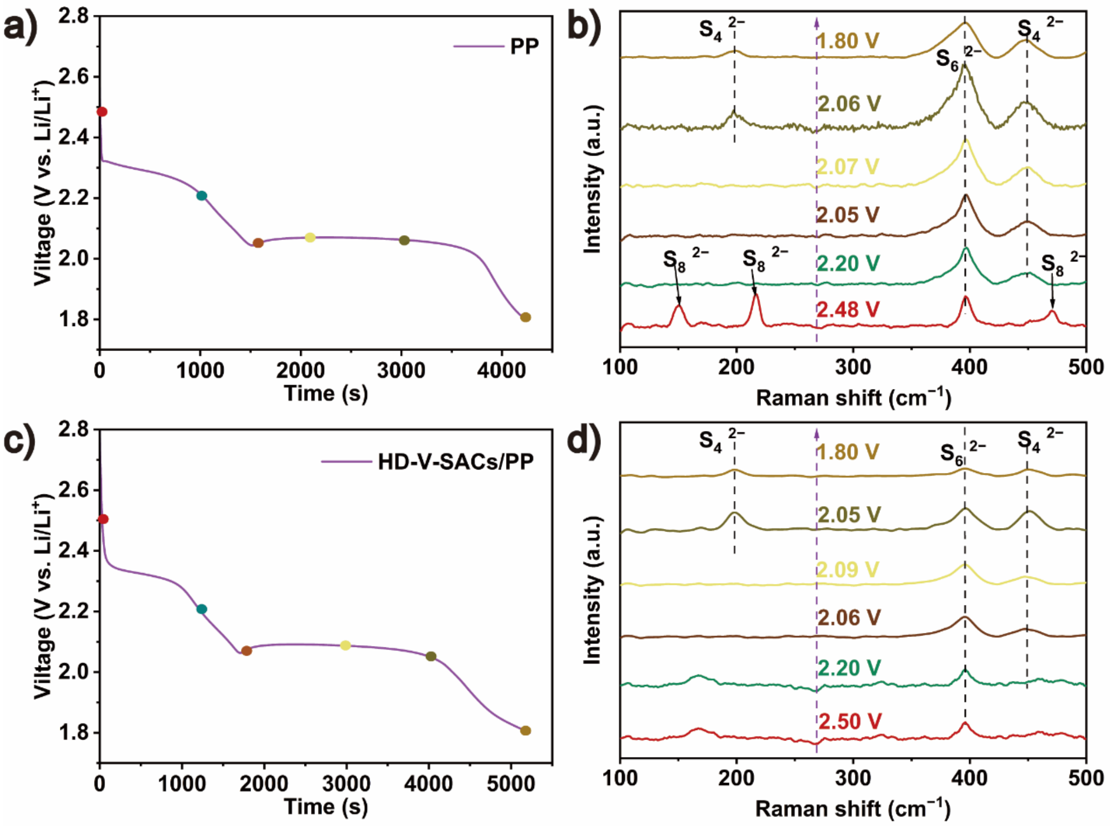

Fig. S12. Time-dependent discharge profiles of the Li-S cells with (a) a pristine PP and (c) a HD-V-SACs/PP as the separator. In-situ Raman spectra acquired from the Li-S cells with (b) a pristine PP and (d) a HD-V-SACs/PP as the separator.

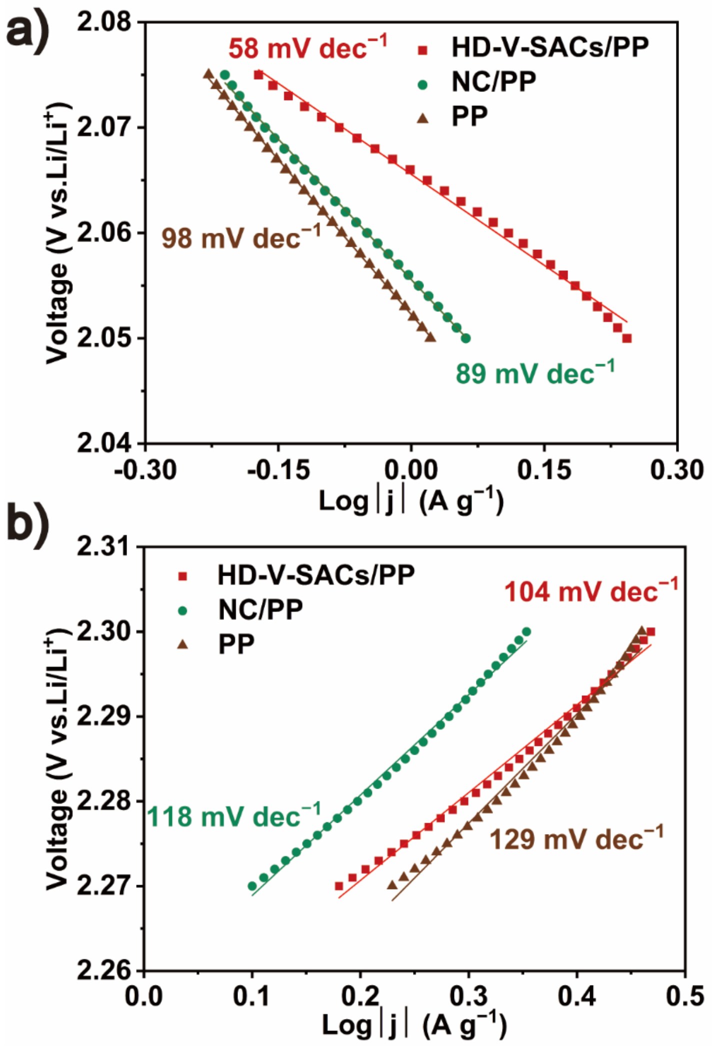

Fig. S13. Tafel plots of (a) the reduction process (peak A in **Fig. 5a**) and (b) the oxidation process (peak B in **Fig. 5a**) of various samples.

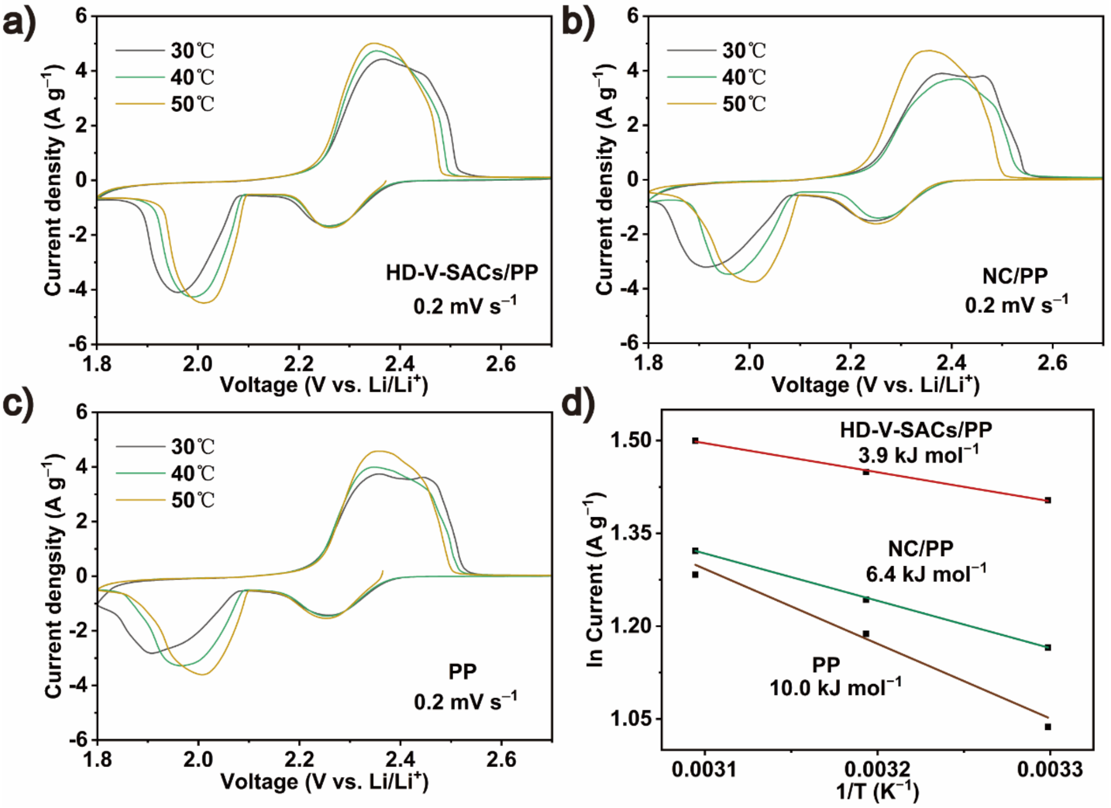

Fig. S14. CV curves of the Li-S cells comprising (a) HD-V-SACs/PP, (b) NC/PP, and (c) pristine PP separators. Scan rate: 0.2 mV s^{-1}. (d) Arrhenius plots of the Li_2S_4 conversion in Li-S cells containing different separators.

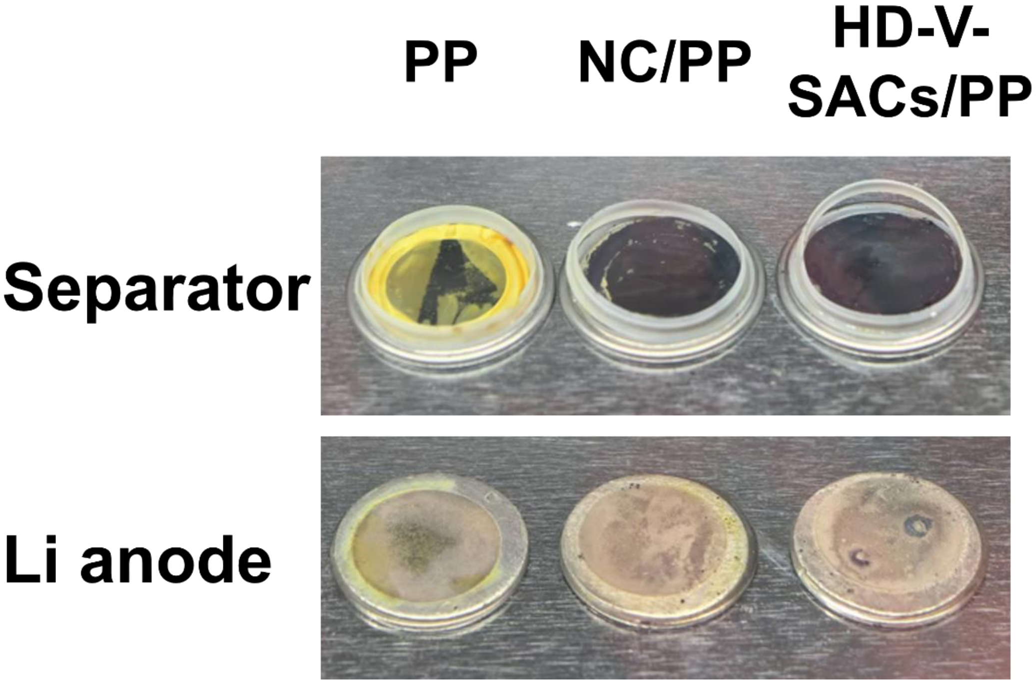

Fig. S15. Digital photographs illustrating the appearance of various separators and the Li anodes in the cells after 100 charge/discharge cycles at 0.5 C.

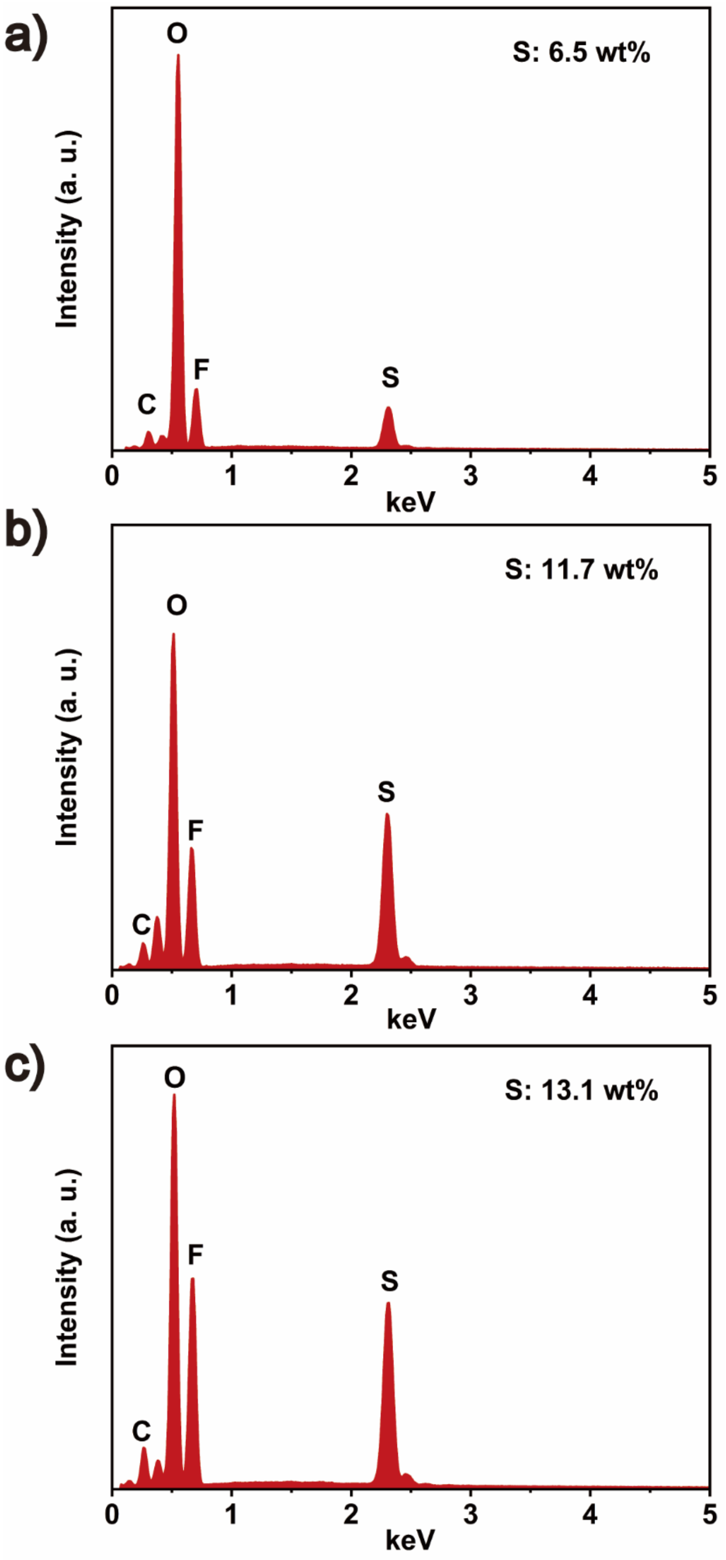

Fig. S16. EDS spectra showing the surface composition of the Li anode in the cells comprising (a) HD-V-SACs/PP, (b) NC/PP, and (c) PP separators after 100 charge/discharge cycles at 0.5 C.

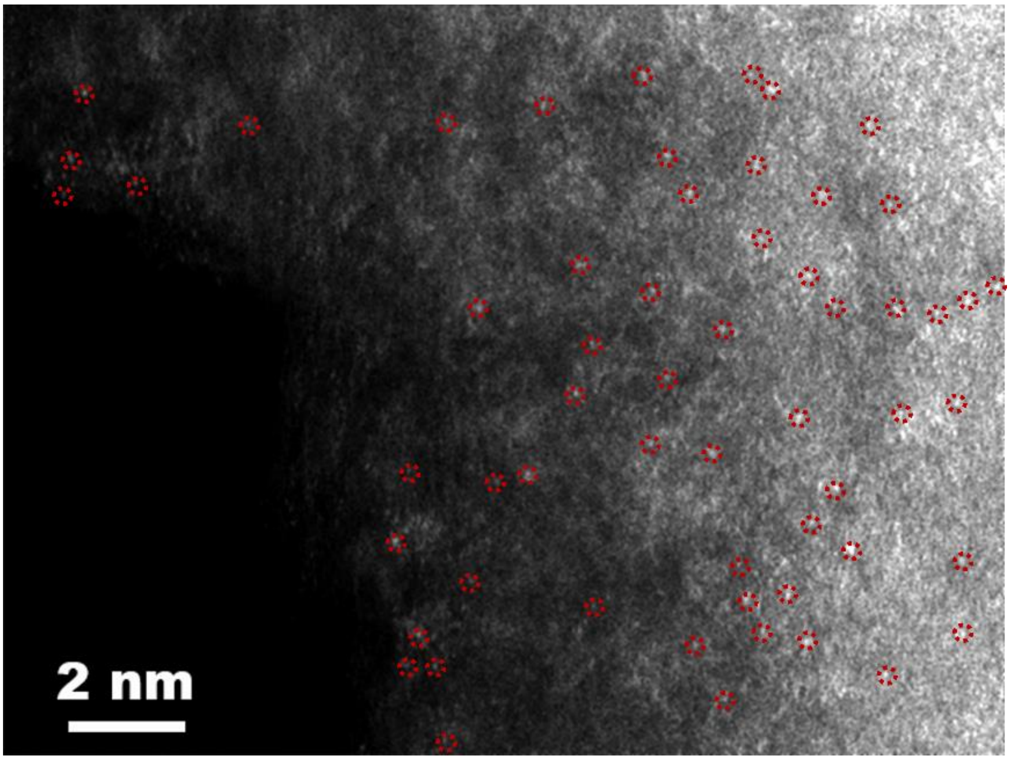

Fig. S17. HAADF-STEM image of the HD-V-SACs in the Li-S cell after 100 charge/discharge cycles at 0.5 C.

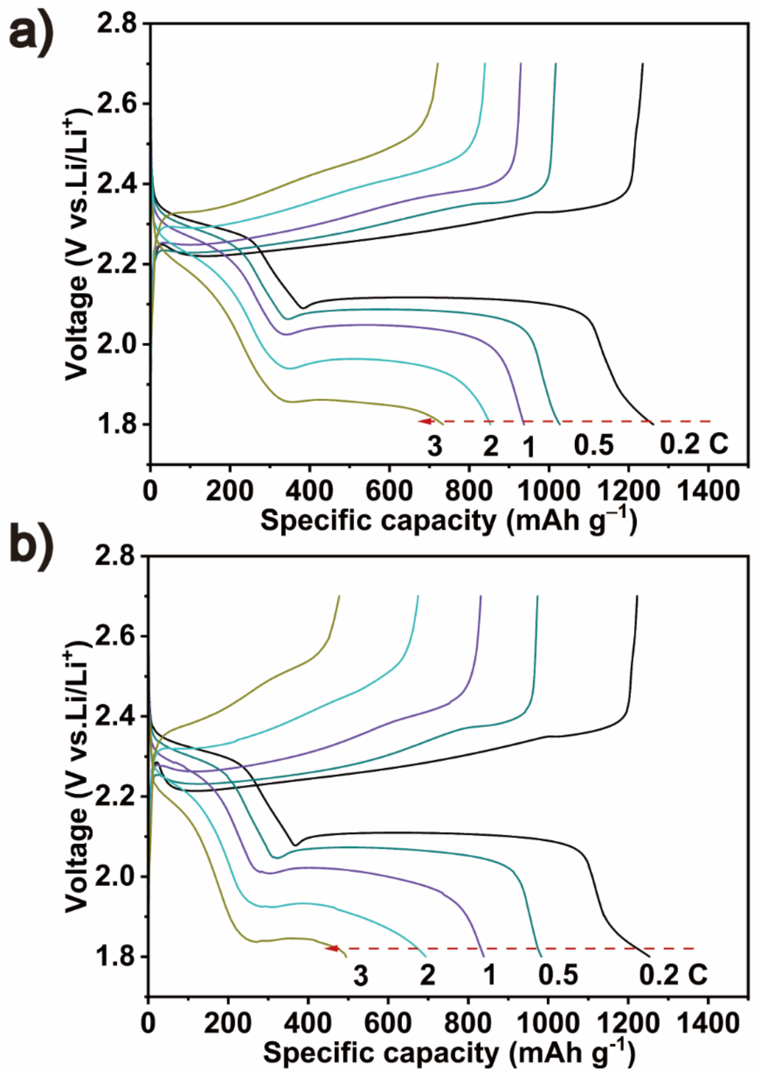

Fig. S18. Galvanostatic charge-discharge profiles at different rates for the cells containing NC/PP and pristine PP separators.

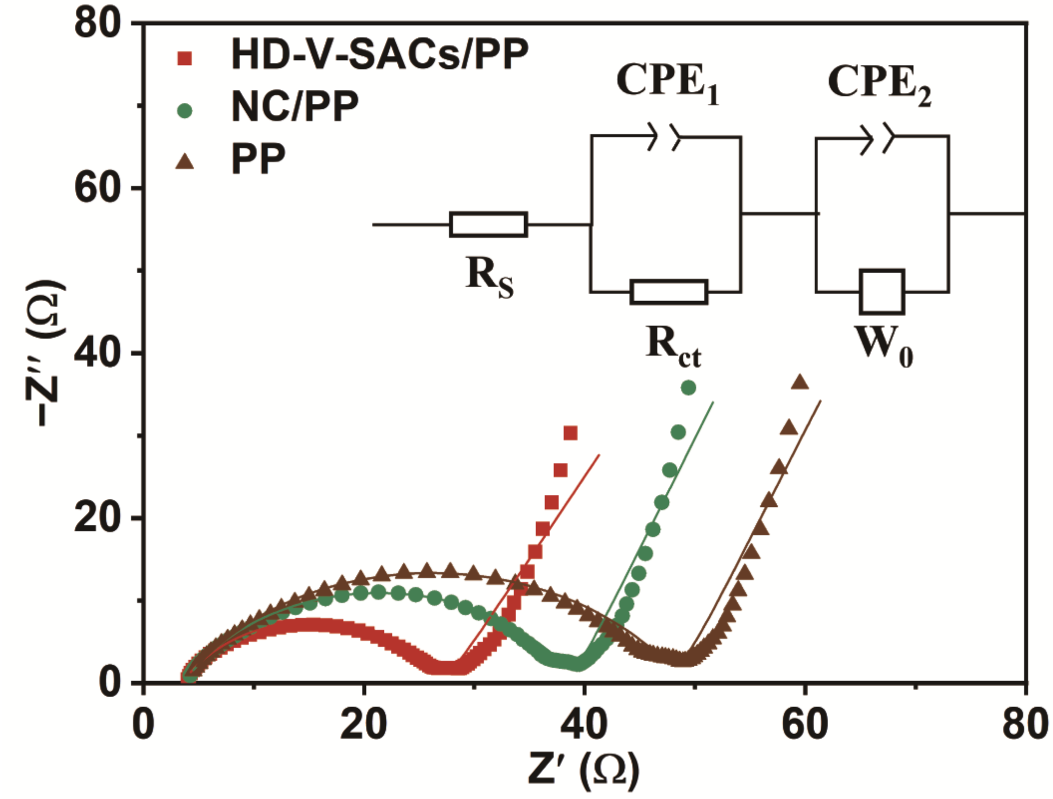

Fig. S19. EIS Nyquist plots of the cells containing HD-V-SACs/PP, NC/PP, and pristine PP separators. The charge transfer resistance (R_{ct}) values for HD-V-SACs/PP, NC/PP, and pristine PP are 24.0 Ω, 35.4 Ω, and 44.9 Ω, respectively.

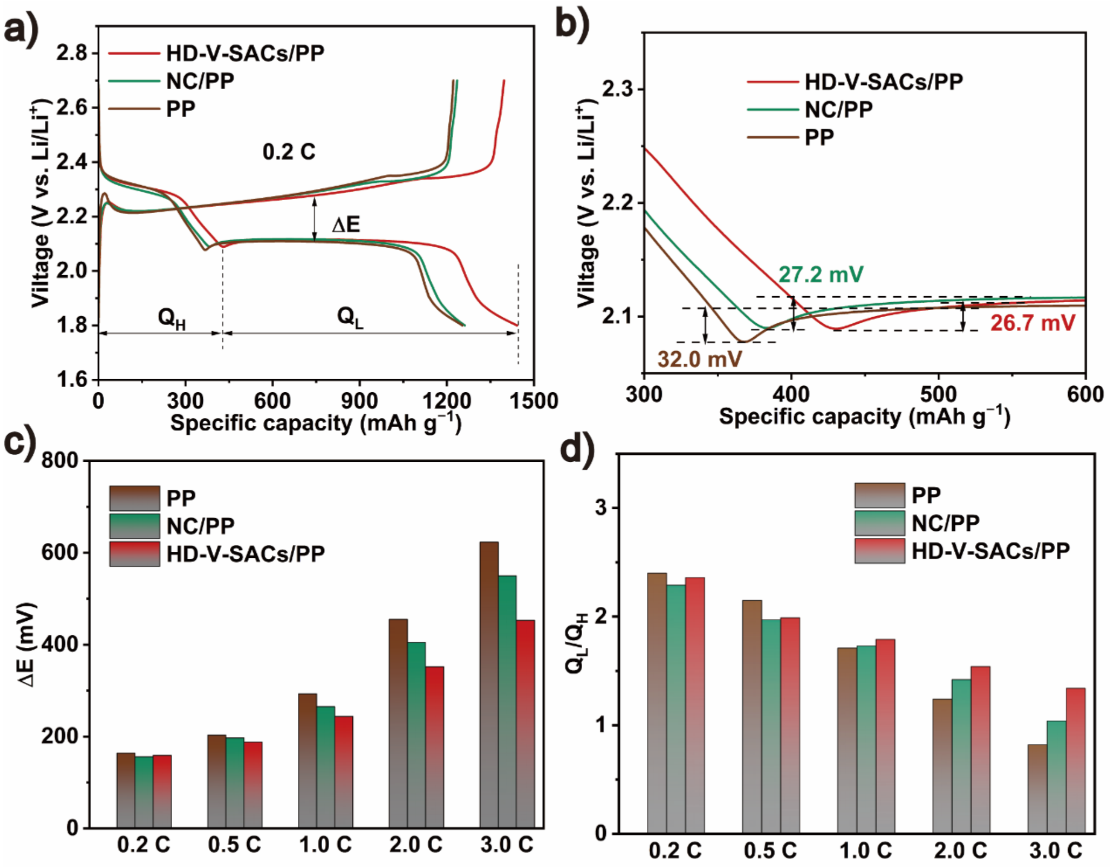

Fig. S20. (a) Galvanostatic charge-discharge profiles of the Li-S cells containing different separators acquired at 0.2 C. (b) Zoomed view in the range of 300 – 600 mAh g^{-1}. The values of (c) ΔE and (d) Q_L/Q_H obtained from the discharge/charge curves at different rates.

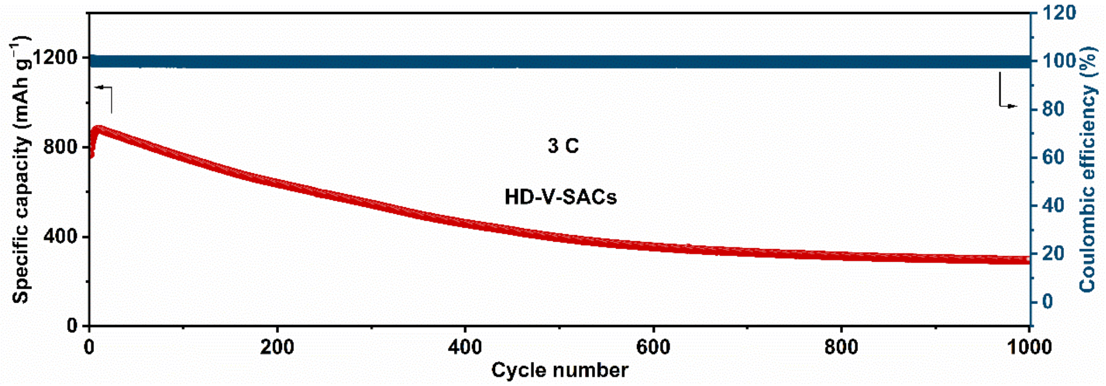

Fig. S21. Long-term cycle stability of Li-S batteries containing the HD-V-SACs/PP separator, tested at 3 C.

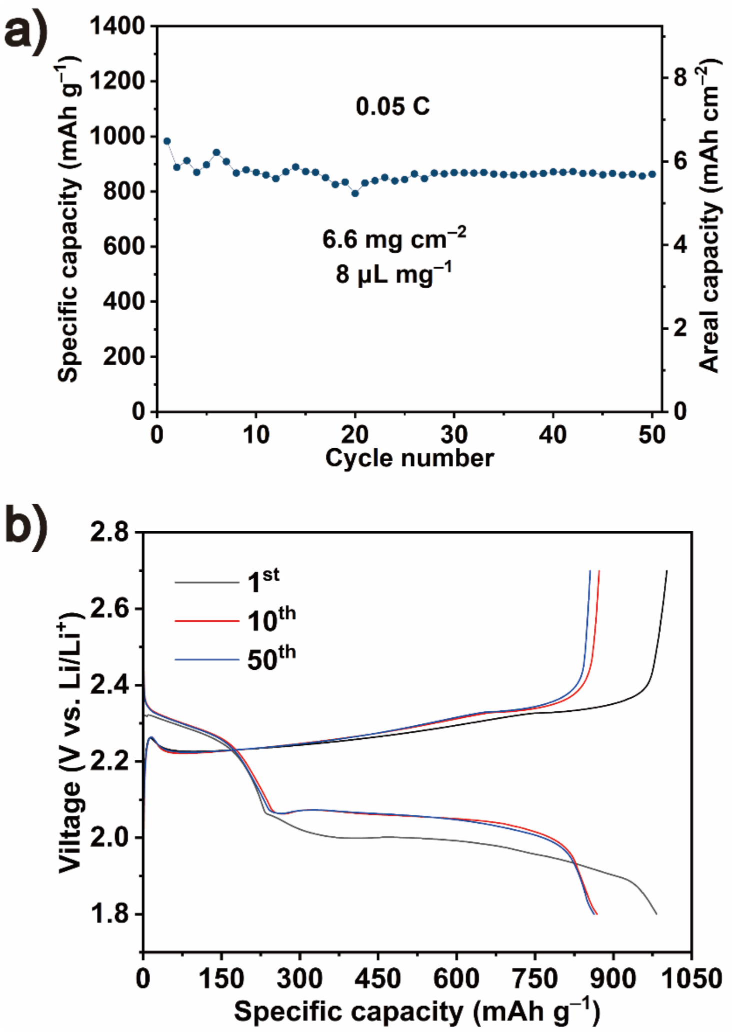

Fig. S22. (a) Cycling performance and (b) galvanostatic charge-discharge profiles of the HD-V-SACs/PP Li-S cell with a high sulfur loading of 6.6 mg cm^{-2} and a low E/S ratio of 8.0 μL mg^{-1}, measured at 0.05 C.

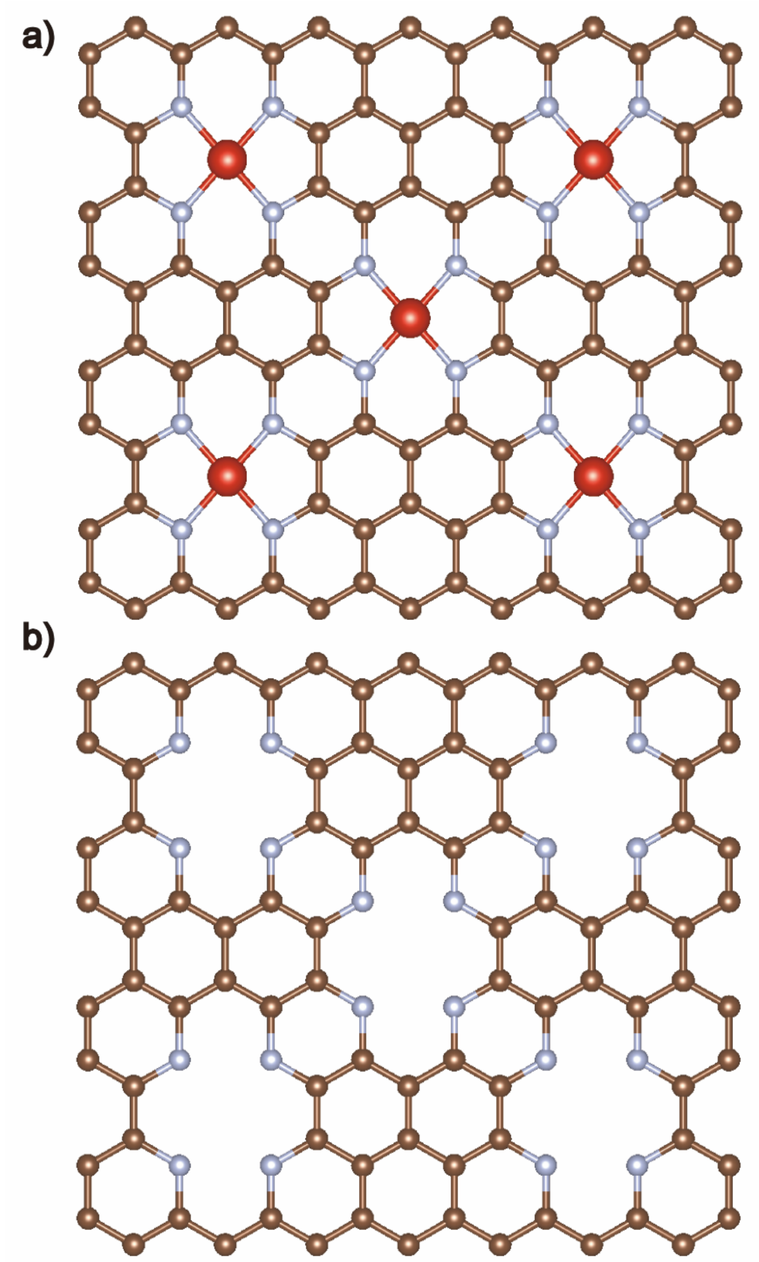

Fig. S23. The optimized models of (a) HD-V-SACs and (b) NC. The brown, grey, and red spheres stand for C, N, and V atoms, respectively.

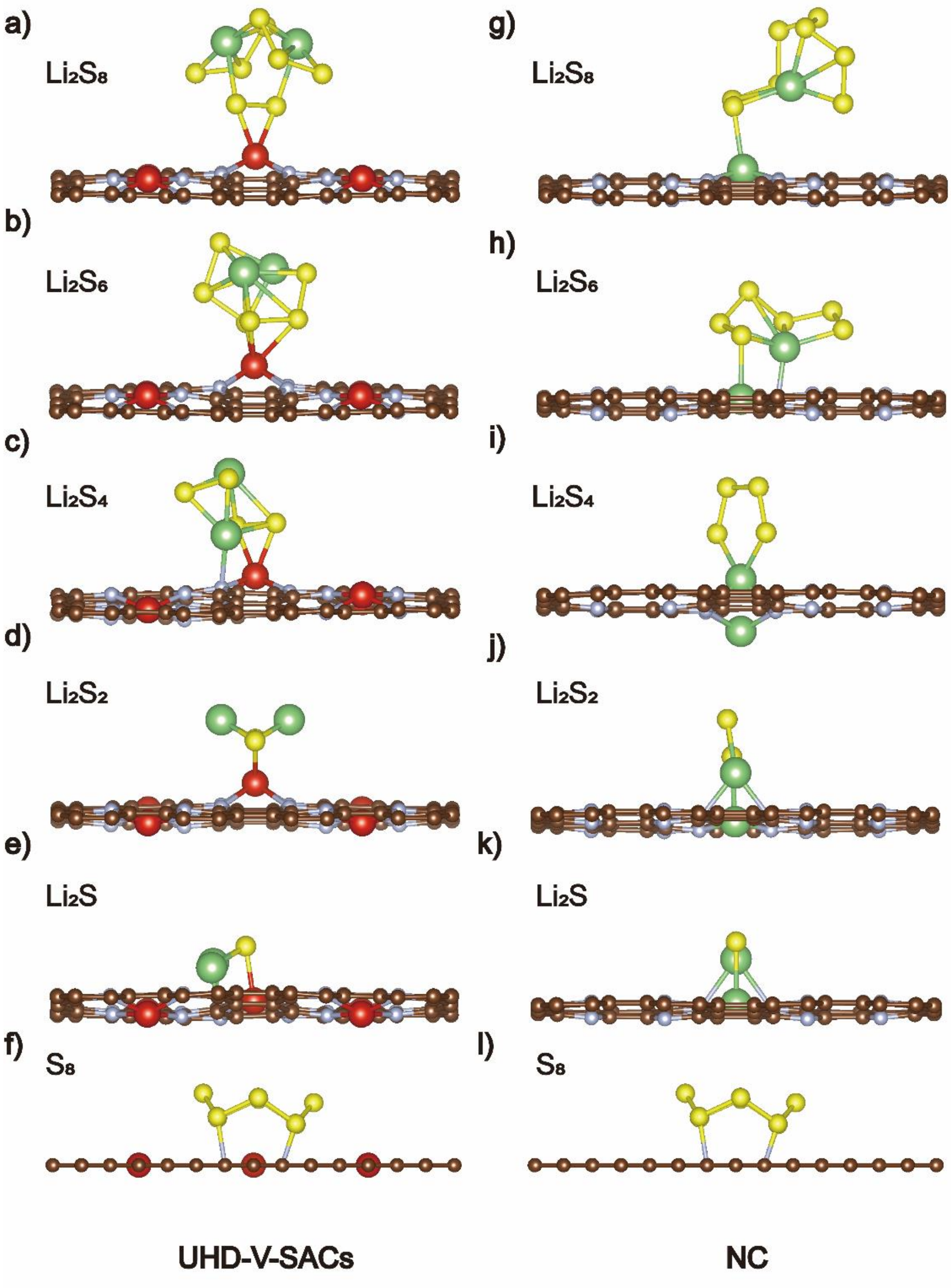

Fig. S24. Side views of the optimized models of (a-e) HD-V-SACs and (f-j) NC adsorbed with different LiPS species. The brown, grey, red, yellow, and green spheres stand for C, N, V, S, and Li atoms, respectively.

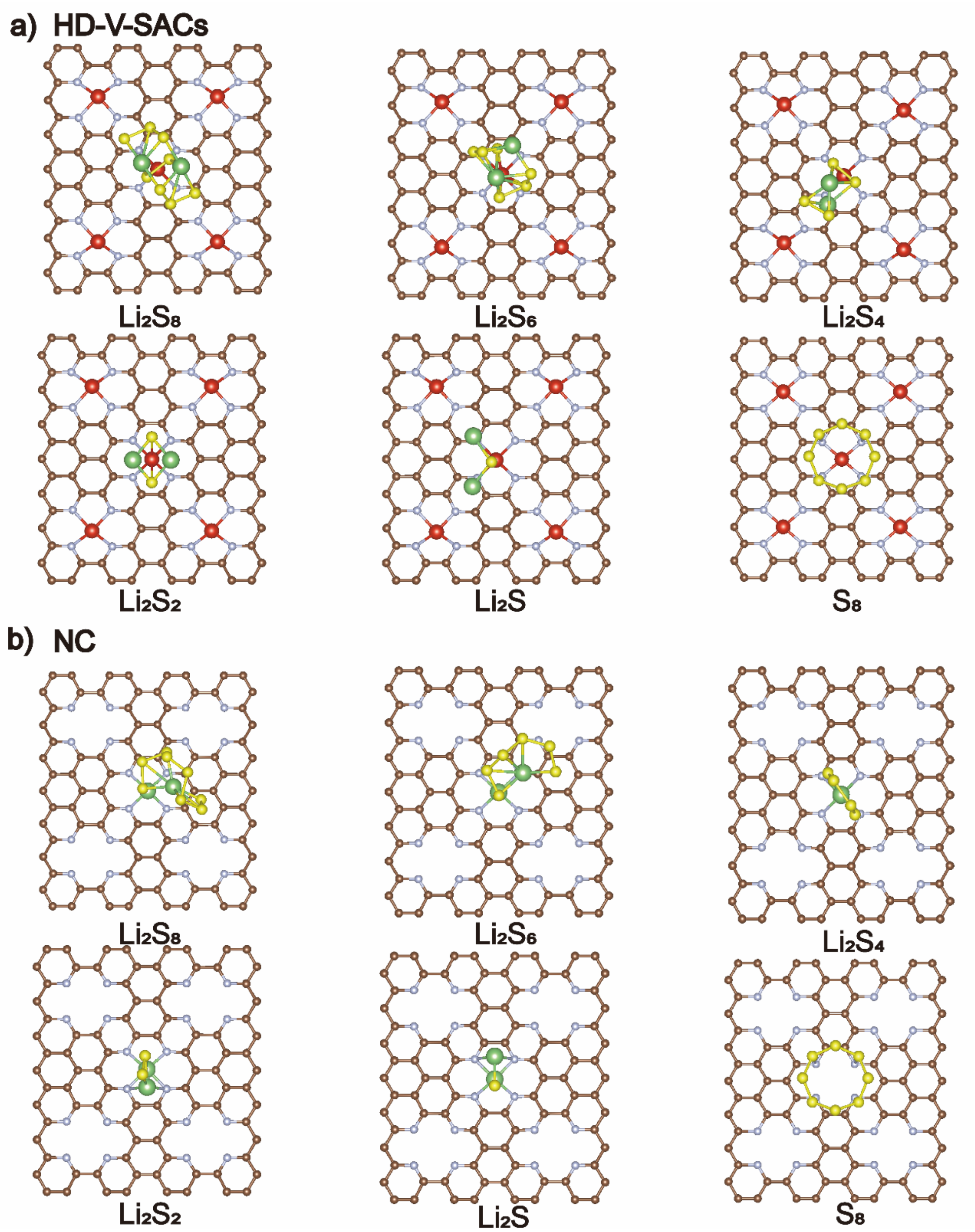

Fig. S25. Top views of the optimized models of (a) HD-V-SACs and (b) NC adsorbed with different LiPS species. The brown, grey, red, yellow, and green spheres stand for C, N, V, S, and Li atoms, respectively.

Supporting Tables

Table S1. Comparison of the loading of V in HD-V-SACs to that in other V-SACs based on N-doped carbon in the literature.

Sample	The loading of V	Ref.
HD-V-SACs	**13.0 wt%**	**This work**
V-SACs-HA	4.3 wt%	S4
V-NC	1.2 wt%	S5
O-V_2-NC	1.3 wt%	S6
3D-PNCV	1.2 wt%	S7
V-NC	12.2 wt%	S8
V-N-C	0.7 at%	S9
N, O-V	0.9 wt%	S10
SAV@NG	4.3 wt%	S11

Table S2. EXAFS fitting parameters of HD-V-SACs sample at the V K-edge

Sample	Shell	CN[a]	*R* factor[b]	σ^2 (Å^2)[c]	*R*(Å)[d]
HD-V-SACs	V-N	3.35	0.0193	0.00099	1.59

[a] *CN* represents the coordination number;

[b] *R* factor indicates the goodness of the fit;

[c] Debye-Waller factor to account for both thermal and structural disorders;

[d] *R* is the distance between absorber and backscattering atoms.

Table S3. Comparison of the electrochemical performance of HD-V-SACs to that of other SACs used as the catalytic coating layer for separators in Li-S batteries reported recently in the literature.

Modified catalytic layer	*S loading (mg cm^{-1})*	*Capacity (mAh g^{-1})*	*Cycle performance (mAh g^{-1})*	*Ref.*
HD-V-SACs	**1.5**	**1016 at 1 C**	**745 after 500 cycles**	**This work**
VN_{1-x}@V-NC	1.5	894 at 1 C	578 after 500 cycles	S5
Co_{SAC}-NPC	1.1 ~ 1.3	986 at 0.5 C	789 after 400 cycles	S12
Co-N_3Cl	0.7 ~ 1.0	804 at 5 C	693 after 600 cycles	S13
Sm-N_3C_3	2.0	1010 at 1 C	731 after 1000 cycles	S14
Co-NPC	1.1	841 at 1 C	601 after 500 cycles	S15
PCN-Cu-MOF	1.6	940 at 1 C	723 after 500 cycles	S16
Fe-N_4/DCS	1.8	969 at 1 C	814 after 500 cycles	S17
FeCoDA-CN	2.5	966 at 1 C	541 after 500 cycles	S18
SA-Co/NGM	1.5	963 at 2 C	731 after 1000 cycles	S19
Fe-N_5/GCNC	0.8 ~ 1.5	769 at 1 C	472 after 1000 cycles	S20
Fe–NSC@GO	2.0	982 at 1 C	768 after 1000 cycles	S21
Ni-NC	1.2	1167 at 1 C	901 after 700 cycles	S22
CoN_5 SA/NC	1.2	1001 at 1 C	786 after 500 cycles	S23
h-Mn-N-C	1.2	952 at 1 C	520 after 1000 cycles	S24

References

S1. H. Park, H. S. Koh and D. J. Siegel, *The Journal of Physical Chemistry C*, 2015, **119**, 4675-4683.

S2. S. Grimme, *Chemistry*, 2012, **18**, 9955-9964.

S3. G. Henkelman, B. P. Uberuaga and H. Jónsson, *The Journal of Chemical Physics*, 2000, **113**, 9901-9904.

S4. Q. Chen, T. Li, H. Huang, W. Wang, Z. Yu, Q. Liu and L. Liu, *Nano Energy*, 2024.

S5. Y. Zhang, C. Ma, C. Zhang, L. Ma, S. Zhang, Q. Huang, C. Liang, L. Chen, L. Zhou and W. Wei, *Chem. Eng. J.*, 2023, **452**, 139410.

S6. L. Wang, Y. Liu, H. Wang, T. Yang, Y. Luo, S. Lee, M. G. Kim, T. T. T. Nga, C. L. Dong and H. Lee, *ACS Nano*, 2023, **17**, 7406-7416.

S7. Y. Jiang, Z. Yu, X. Zhou, X. Cheng, H. Huang, F. Liu, Y. Yang, S. He, H. Pan, H. Yang, Y. Yao, X. Rui and Y. Yu, *Adv. Mater.*, 2023, **35**, e2208873.

S8. X. Hai, S. Xi, S. Mitchell, K. Harrath, H. Xu, D. F. Akl, D. Kong, J. Li, Z. Li, T. Sun, H. Yang, Y. Cui, C. Su, X. Zhao, J. Li, J. Perez-Ramirez and J. Lu, *Nat. Nanotechnol.*, 2022, **17**, 174-181.

S9. S. Yu, Y. Sun, L. Song, X. Cao, L. Chen, X. An, X. Liu, W. Cai, T. Yao, Y. Song and W. Zhang, *Nano Energy*, 2021, **89**, 106414.

S10. L. Cheng, H. Huang, Z. Lin, Y. Yang, Q. Yuan, L. Hu, C. Wang and Q. Chen, *J Colloid Interface Sci*, 2021, **594**, 466-473.

S11. G. Zhou, S. Zhao, T. Wang, S. Z. Yang, B. Johannessen, H. Chen, C. Liu, Y. Ye, Y. Wu, Y. Peng, C. Liu, S. P. Jiang, Q. Zhang and Y. Cui, *Nano Lett.*, 2020, **20**, 1252-

1261.

S12. F.-J. Lin, C.-L. Huang, X.-Y. Jiang, J.-Q. Liao and Y.-Y. Li, *ACS Sustainable Chemistry & Engineering*, 2024, **12**, 3478-3490.

S13. F. Cao, X. Zhang, Z. Jin, J. Zhang, Z. Tian, D. Kong, Y. Li, Y. Li and L. Zhi, *Advanced Energy Materials*, 2024, **14**.

S14. R. Zhou, Y. Ren, W. Li, M. Guo, Y. Wang, H. Chang, X. Zhao, W. Hu, G. Zhou and S. Gu, *Angew Chem Int Ed Engl*, 2024, **63**, e202405417.

S15. Z. Wang, Y. Cheng, S. Wang, J. Xu, B. Peng, D. Luo and L. Ma, *Nano Research*, 2023, **16**, 9335-9343.

S16. X. Li, Y. Xiao, Q. Zeng, L. Xu, S. Guo, C. Zheng, Q. Zhang and S. Huang, *Nano Energy*, 2023, **116**.

S17. W. Jing, Q. Tan, Y. Duan, K. Zou, X. Dai, Y. Song, M. Shi, J. Sun, Y. Chen and Y. Liu, *Small*, 2023, **19**, e2204880.

S18. P. Song, S. Zheng, Z. Ullah, Z. Yang, P. Zhu, A. He, C. Wang and Q. Li, *ACS Applied Energy Materials*, 2023, **6**, 4671-4682.

S19. D. Wang, K. Ma, J. Hao, W. Zhang, H. Shi, C. Wang, Z. Xiong, Z. Bai, F.-R. Chen, J. Guo, B. Xu, X. Yan and Y. Gu, *Chem. Eng. J.*, 2023, **466**, 143182.

S20. S. He, J. Yang, S. Liu, X. Wang, X. Che, M. Wang and J. Qiu, *Chem. Eng. J.*, 2023, **454**, 140202.

S21. L. Ren, J. Liu, Y. Zhao, Y. Wang, X. Lu, M. Zhou, G. Zhang, W. Liu, H. Xu and X. Sun, *Adv. Funct. Mater.*, 2023, **33**, 2210509.

S22. R. Wang, J. Qin, F. Pei, Z. Li, P. Xiao, Y. Huang, L. Yuan and D. Wang, *Advanced*

Functional Materials, 2023, **33**, 2305991.

S23. F. Zhang, Z. Tang, T. Zhang, H. Xiao, H. Zhuang, X. Liang, L. Zheng and Q. Gao, *J. Mater. Chemistry A*, 2022, **10**, 22114-22124.

S24. S. Qiao, D. Lei, Q. Wang, X. Shi, Q. Zhang, C. Huang, A. Liu, G. He and F. Zhang, *Chem. Eng. J.*, 2022, **442**, 136258.